Uncertainty in Forced and Natural Arctic Solar Absorption Variations in CMIP6 Models

Anne Sledd[a] and Tristan L'Ecuyer[a]

[a] *University of Wisconsin–Madison, Madison, Wisconsin*

ABSTRACT: The Arctic is rapidly changing, with increasingly dramatic sea ice loss and surface warming in recent decades. Shortwave radiation plays a key role in Arctic warming during summer months, and absorbed shortwave radiation has been increasing largely because of greater sea ice loss. Clouds can influence this ice–albedo feedback by modulating the amount of shortwave radiation incident on the Arctic Ocean. In turn, clouds impact the amount of time that must elapse before forced trends in Arctic shortwave absorption emerge from internal variability. This study determines whether the forced climate response of absorbed shortwave radiation in the Arctic has emerged in the modern satellite record and global climate models. From 18 years of satellite observations from CERES-EBAF, we find that recent declines in sea ice are large enough to produce a statistically significant trend (1.7×10^6 PJ or 3.9% per decade) in observed clear-sky absorbed shortwave radiation. However, clouds preclude any forced trends in all-sky absorption from emerging within the existing satellite record. Across 18 models from phase 6 of the Coupled Model Intercomparison Project (CMIP6), the predicted time to emergence of absorbed shortwave radiation trends varies from 8 to 39 and from 8 to 35 years for all-sky and clear-sky conditions, respectively, across two future scenarios. Furthermore, most models fail to reproduce the observed cloud delaying effect because of differences in internal variability. Contrary to observations, one-third of models suggest that clouds may reduce the time to emergence of absorbed shortwave trends relative to clear skies, an artifact that may be the result of inaccurate representations of cloud feedbacks.

KEYWORDS: Arctic; Climate change; Clouds; Shortwave radiation; Climate variability

1. Introduction

The Arctic is one of the most rapidly changing regions on Earth. Sea ice loss has been observed in all months since the beginning of the satellite era (Onarheim et al. 2018) with many regions transitioning from perennial to seasonal ice cover in recent years (Comiso 2002). The remaining sea ice is younger and thinner (Stroeve et al. 2012; Lindsay and Schweiger 2015) as its decline accelerates (Comiso et al. 2008). As sea ice has decreased, Arctic surface air temperatures have increased by almost 2°C over the last century (Box et al. 2019). This warming is more than 2 times as large as the global average, a phenomenon known as Arctic amplification (AA) (Serreze et al. 2009). AA is driven by various feedback mechanisms that manifest themselves through changes in the Arctic energy budget (Serreze and Barry 2011). One such mechanism is the ice-albedo feedback, in which reduced sea ice lowers the surface albedo and allows more shortwave (SW) radiation to be absorbed, further melting additional sea ice (Curry et al. 1995) both by warming sea surface temperatures (Steele et al. 2008) and increasing heat release in autumn and winter that delays sea ice growth (Tietsche et al. 2011).

Some of the most dramatic changes in the Arctic have been observed over the last two decades. A marked transition in the annual cycle of sea ice cover has altered the behavior of surface–atmosphere heat and moisture exchanges, declared the "new Arctic" by some (Carmack et al. 2015). The rapid changes in Arctic climate since 2000, coupled with the golden age of satellite observations in polar regions, motivate a deeper investigation into how seasonal trends in sea ice cover and thickness may be influencing solar absorption in the Arctic Ocean. Figure 1 shows deseasonalized anomalies of monthly Northern Hemisphere sea ice extent from the National Snow and Ice Data Center (NSIDC) and surface albedo and planetary albedo calculated using clear-sky and all-sky SW fluxes, respectively, from Clouds and Earth's Radiant Energy System Energy Balance and Filled (CERES-EBAF) over the area above 60°N from 2001 to 2017. Reliable top-of-atmosphere (TOA) fluxes have only been available in the Arctic since the launch of CERES, limiting time series analysis of Arctic energy changes using observations. However, even over this relatively short time period there are significant negative trends in sea ice extent and surface albedo anomalies. The time series of surface albedo anomalies closely follows that of sea ice extent, as is expected given the high albedo of sea ice and its marked transition to low albedo ocean. On the other hand, anomalies in the planetary albedo derived from TOA fluxes are, to some degree, disconnected from sea ice extent. For example, September 2012 had the lowest sea ice extent recorded during the satellite era, and the reduced sea ice in turn clearly lowered the surface albedo. Viewed from space, however, the September 2012 decline in TOA albedo was less than half that at the surface. This disconnection is largely due to clouds in the intervening atmosphere that are observed to modulate the influence of surface

---

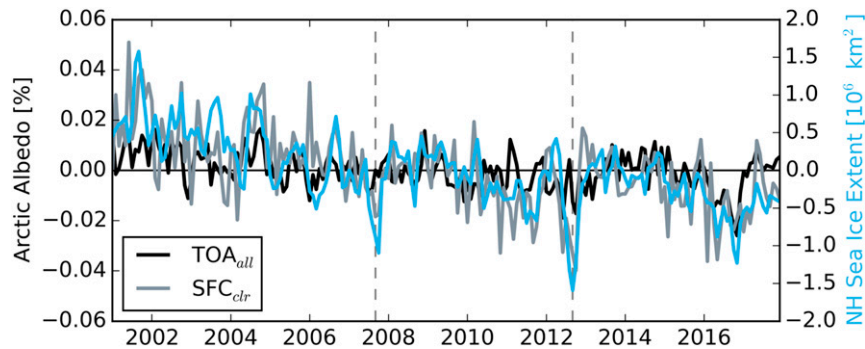*Corresponding author*: Anne Sledd, sledd@wisc.edu

FIG. 1. Monthly deseasonalized anomalies for Arctic surface (SFC) and top-of-atmosphere (TOA) albedos and Northern Hemisphere (NH) sea ice extent (SIE) from 2001 to 2017. Albedos are calculated using fluxes from CERES-EBAF Ed 4.1, and SIE estimates are from the NSIDC. Dashed vertical lines mark September 2007 and 2012, the lowest SIE on record. The surface albedo anomalies closely track the SIE anomalies, and both exhibit clear negative trends over this time period. TOA albedo anomalies, on the other hand, are often decoupled from the surface, and the trend is much more difficult to discern.

albedo on the TOA albedo by as much as a factor of 2 (Sledd and L'Ecuyer 2019).

Clouds are an important control on the Arctic energy budget. SW radiation, in particular, is strongly modulated by cloud cover and cloud microphysical properties (e.g., Sedlar et al. 2011). In fact, the atmosphere contributes far more to the planetary albedo than the surface both globally (Donohoe and Battisti 2011) and in the Arctic (Qu and Hall 2005) where it accounts for at least 75% of the TOA albedo. Clouds are a determining factor in how much SW radiation is reflected back to space compared to how much actually reaches the surface (Stephens et al. 2015). While reduced sea ice has been linked to lower surface and planetary albedo (Pistone et al. 2014), clouds reduce the impact of sea ice loss on the planetary albedo in the Arctic (Gorodetskaya et al. 2008). This damping effect of clouds reduces the sensitivity of the planetary albedo to changes in sea ice and snow cover by half relative to the surface albedo (Sledd and L'Ecuyer 2019). In turn, the masking effect of clouds explains why they reduce the strength of the ice-albedo feedback (Soden et al. 2008; Hwang et al. 2018) and why, unlike sea ice extent and surface albedo, it is more difficult to discern a trend in the TOA albedo in Fig. 1. This suggests that a longer data record may be required to discern the forced climate trends in all-sky absorbed SW radiation.

Because clouds strongly influence the planetary albedo and, therefore, how much SW radiation reaches the surface, the future of clouds is critical to the future of the Arctic climate (Kay et al. 2016). Observational studies have found some evidence that increased cloud cover may offset decreases in surface albedo in the Arctic (Kato et al. 2006; Katlein et al. 2017), although trends in cloud cover are small and seasonally dependent (Wang et al. 2012; Kay and Gettelman 2009). These studies have also relied on satellites with passive sensors that struggle to identify cold bright clouds over cold bright surfaces in the Arctic. While data from active sensors (e.g., radar and lidar aboard *CloudSat* and

CALIPSO) have greatly improved our understanding of cloud processes in the Arctic (Kay and L'Ecuyer 2013; Morrison et al. 2018) they have only been in orbit since 2006 and suffer from limited nadir sampling.

Global climate models (GCMs), on the other hand, allow the bulk effects of various forcing and feedback mechanisms to be analyzed with a plethora of prognostic and diagnostic variables that span for far longer time periods than observations. However, studying the future of polar climate using GCMs presents its own challenges due to ongoing difficulties accurately representing modern-day cloud processes and feedbacks (Li et al. 2013; Dolinar et al. 2015). It is not just the amount of cloud cover that is important to simulate correctly, but also the phase and water content of clouds that govern their influence on the Arctic radiation balance (Shupe and Intrieri 2004). Differences in cloud parameterizations have thus led to biases, relative to satellite and ground observations, in the SW energy budget in GCMs (Gorodetskaya et al. 2006). While progress has been made studying cloud feedbacks in the Arctic (e.g., Morrison et al. 2019), the challenge of realistically representing clouds persists across generations of GCMs (Vignesh et al. 2020), casting uncertainty on projected rates of AA and accompanying Arctic sea ice loss.

Understanding recent changes in the Arctic is key to correctly assessing how it may change in the future. This paper utilizes the growing record of satellite-based Earth radiation budget observations and a statistical framework for assessing the time to emergence (TTE) of forced climate trends in the Arctic. We combine these tools to establish whether the recent observational record is long enough to distinguish forced changes in absorbed SW radiation in the Arctic from interannual variability with statistical confidence and to understand how clouds impact our ability to discern such trends. We further examine the character of Arctic absorbed SW radiation trends in modern climate models. Specifically, we address the following questions: 1) how do clouds impact

trends in absorbed SW radiation and their TTE? 2) how do predicted SW trends in GCMs compare to observations? and 3) what aspects of modeled Arctic climate variability drive differences in TTE relative to observations? We estimate the TTE of absorbed SW radiation trends from satellite observations and GCMs from phase 6 of the Coupled Model Intercomparison Project (CMIP6) over the twenty-first century. A mathematical understanding of the factors that influence SW trend detection is presented and then related to the physical changes occurring in today's Arctic.

2. Methods

a. Datasets

1) OBSERVATIONS

Both observational datasets used in this study are extracted from the Arctic Observations and Reanalysis Integrated System (ArORIS), a collection of datasets created to support Arctic climate research (Christensen et al. 2016). All datasets in ArORIS are regridded to a uniform $2.5° \times 2.5°$ grid and averaged to monthly time scales.

We use radiative fluxes from the CERES-EBAF edition 4.1 on board the *Terra* and *Aqua* NASA satellites. TOA fluxes in the CERES-EBAF dataset are adjusted within their ranges of uncertainty to be consistent with the global heating rate from in situ ocean observations (Loeb et al. 2018; Kato et al. 2018). We use all-sky fluxes at the TOA and total-region clear-sky fluxes at the surface. Previously, clear-sky fluxes from CERES only represented fluxes in areas that were free of clouds at the time of observation. Total-region clear-sky fluxes are intended to facilitate direct comparisons with models that typically determine clear-sky fluxes over a grid box by ignoring clouds in the atmospheric column in the radiative transfer calculation. To that end, CERES total-region clear-sky fluxes include an adjustment factor given by the difference of calculating clear-sky fluxes for cloud-free regions and calculating them with a radiative transfer model while ignoring clouds in the atmospheric column (Loeb et al. 2020). Uncertainty for net SW flux at the TOA under all-sky conditions is $2.5 \, \text{W m}^{-2}$ (Loeb et al. 2018). At the surface under clear-sky conditions in the Arctic, uncertainty in SW fluxes is 14 and $16 \, \text{W m}^{-2}$ for downwelling and upwelling radiation, respectively (Kato et al. 2018).

Sea ice concentrations (SIC) and extent are derived from the NSIDC Equal-Area Scalable Earth grid (EASE) weekly product (Brodzik and Armstrong 2013). Their long-term record of SIC dating back to 1978 is estimated using brightness temperature from the *Nimbus-7* Scanning Multichannel Microwave Radiometer (SMMR), the Defense Meteorological Satellite Program (DMSP) *F8*, *F11*, and *F13* Special Sensor Microwave/Imagers (SSM/Is), and the DMSP *F17* Special Sensor Microwave Imager/Sounder (SSMIS). We use SIC to calculate sea ice area (SIA) by multiplying the SIC in each grid box by its area and summing over the Arctic, defined as the area north of the Arctic Circle (66.5°N).

2) CMIP6

To investigate the changes in SW absorption beyond our observational record, we analyze the output of 18 models participating in CMIP6 (Eyring et al. 2016), listed in Table 1. We use the historical forcing run, which covers the years from 1850 to 2014, and two shared societal pathways (SSPs) from the ScenarioMIP deck. We compare SSP2 ("middle of the road" scenarios with moderate population and economic growth) with an end-of-century radiative forcing of $4.5 \, \text{W m}^{-2}$ (SSP245) and SSP5 ("business as usual" scenarios with strong economic growth relying on fossil fuels) with radiative forcing of $8.5 \, \text{W m}^{-2}$ (SSP585) (O'Neill et al. 2016). These scenarios include years 2015–2100. The first ensemble member (r1i1p1f1) is used from each model, and the native resolution of each model is kept before each variable is averaged or summed over the Arctic. Variables that are averaged (e.g., total cloud fraction, surface air temperature) are weighted by grid box area, while most other variables are cumulative (e.g., sea ice area) and are summed over the Arctic. For grid boxes that contain the Arctic Circle, the area is recalculated such that only the area north of 66.5°N is included in the sum or average.

b. Statistical methods

1) TIME TO EMERGENCE

This analysis uses the detection of statistically significant forced responses in time series that include natural variability to query the existence of observed SW absorption trends in the Arctic and evaluate their representation in modern GCMs. While hypothesis testing can determine when a trend is different from zero for a chosen confidence level, it does not take into account variance or autocorrelation that are common in geophysical time series. In the 1990s, Tiao et al. (1990) and Weatherhead et al. (1998) published methods for trend detection in geophysical applications that take these issues into account. Their methods of trend detection first assume the time series of interest can be modeled as the sum of a mean state with a linear trend ω and noise. The noise is assumed to be an autoregressive order-one [AR(1)] process with lag-1 autocorrelation ϕ and variance σ^2. The common variance (of the random fluctuations about zero in the noise that is assumed to be a white noise process) σ_e^2 is related to the variance of the noise by

$$\sigma_e^2 = \text{Variance}(N_t) = \sigma_N^2(1 - \phi^2). \tag{1}$$

The variance and autocorrelation are calculated from the detrended time series of anomalies.

As in Weatherhead et al. (1998) and Chepfer et al. (2018), we consider a trend to have emerged at the 95% confidence level when it is at least twice as large as the standard deviation of the measured trend: $|\hat{\omega}/\sigma_{\hat{\omega}}| > 2$. The standard deviation of the trend $\sigma_{\hat{\omega}}$ can be approximated as

$$\sigma_{\hat{\omega}} \approx \sigma_N \left[\frac{12 \, dt}{T^3} \frac{(1 + \phi)}{(1 - \phi)} \right]^{1/2}, \tag{2}$$

where T is the length of the time series and dt is the time interval—in our case $dt = 1$ for our annual observations discussed more below. This equation is adapted for annual time

TABLE 1. Models included from phase 6 of the Coupled Model Intercomparison Project. Most model expansions can be found online (https://www.ametsoc.org/PubsAcronymsList).

Model	Modeling center	ATM grid (lon/lat)	OCN grid (lon/lat)
ACCESS-CM2	Commonwealth Scientific and Industrial Research Organisation	192×144	360×300
ACCESS-ESM1.5	Commonwealth Scientific and Industrial Research Organisation	192×145	360×300
BCC-CSM2-MR	Beijing Climate Center	320×160	360×232
CESM2	National Center for Atmospheric Research	288×192	320×384
CESM2(WACCM)	National Center for Atmospheric Research	288×192	320×384
CanESM5	Canadian Centre for Climate Modelling and Analysis	128×64	361×290
EC-Earth3	EC-Earth Consortium	512×256	362×292
EC-Earth3-Veg	EC-Earth Consortium	512×256	362×292
GFDL-ESM4	NOAA Geophysical Fluid Dynamics Laboratory	360×180	720×576
INM-CM4.8	Institute of Numerical Mathematics	180×120	360×318
INM-CM5.0	Institute of Numerical Mathematics	180×120	720×720
IPSL-CM6A-LR	Institut Pierre-Simon Laplace	144×143	362×332
MIROC6	Japan Agency for Marine-Earth Science and Technology	256×128	360×256
MPI-ESM1.2-LR	Max Planck Institute for Meteorology	192×96	256×220
MPI-ESM1.2-HR	Max Planck Institute for Meteorology	384×192	802×404
MRI-ESM2	Meteorological Research Institute	320×160	128×64
NESM3	Nanjing University of Information Science and Technology	192×96	362×292
NorESM2-LM	Norwegian Climate Center	144×96	360×384

series, based on Lian (2017), from its original form using monthly time series ($dt = 1/12$).

The time to emergence (TTE) is defined as how many years of observations are needed for a measured trend to be statistically significant. For a given time series, a trend is calculated and tested for significance over intervals of increasing length, for example, $[0, dt]$, $[0, 2dt]$, $[0, 3dt]$, ... , $[0, T]$. The confidence for each time interval is calculated from Eq. (2); the trend has emerged when it remains greater than two. This process is shown in Fig. 2 for an ensemble of synthetic time series, discussed shortly.

Chepfer et al. (2018) demonstrate that such an analysis provides a statistical basis for determining how long it takes forced climate changes to emerge from interannual variability in observational data records. Similar techniques were used to project trend detection of broadband and spectral albedos (Feldman et al. 2011) and to inform instrument requirements for future climate monitoring satellite missions (Wielicki et al. 2013). When applied to global mean TOA irradiances, Phojanamongkolkij et al. (2014) found no discernible trend over 2000–11 in reflected SW or emitted longwave radiation from CERES.

2) SYNTHETIC TIME SERIES

As in Chepfer et al. (2018) we combine TTE with synthetic time series to estimate the time needed for trends to be measurably greater than the climate variability. Synthetic

time series are created that maintain the statistical behavior (autocorrelation and variance) of the original time series.

To calculate these synthetic time series, we again assume the data can be represented by the sum of a linear trend and noise. We take the variance calculated from Eq. (1) and generate a series of random noise with zero mean from it. On top of this noise, we can add a linear trend, illustrated in Fig. 2a. Synthetic time series are continued to 150 years, which is long enough for trends from all CMIP6 models to emerge under both SSP245 and SSP585. Synthetic ensembles are composed of 300 individual time series. This process can be applied to models as well as observations to create ensembles of time series. While large ensembles from GCMs are an incredibly powerful tool for determining shifts in climate beyond the inherent internal variability (e.g., Onarheim and Årthun 2017), the authors know of no way to create a true large ensemble from observations as can be done with GCMs. Using synthetic time series also allows us to examine GCMs that do not have large ensembles associated with them, expanding the number of models available for analysis.

3) ACCUMULATED ABSORBED SHORTWAVE RADIATION

The strong seasonality of the Arctic poses unique challenges for time series analysis. As mentioned earlier, this trend detection method is predicated on the assumption
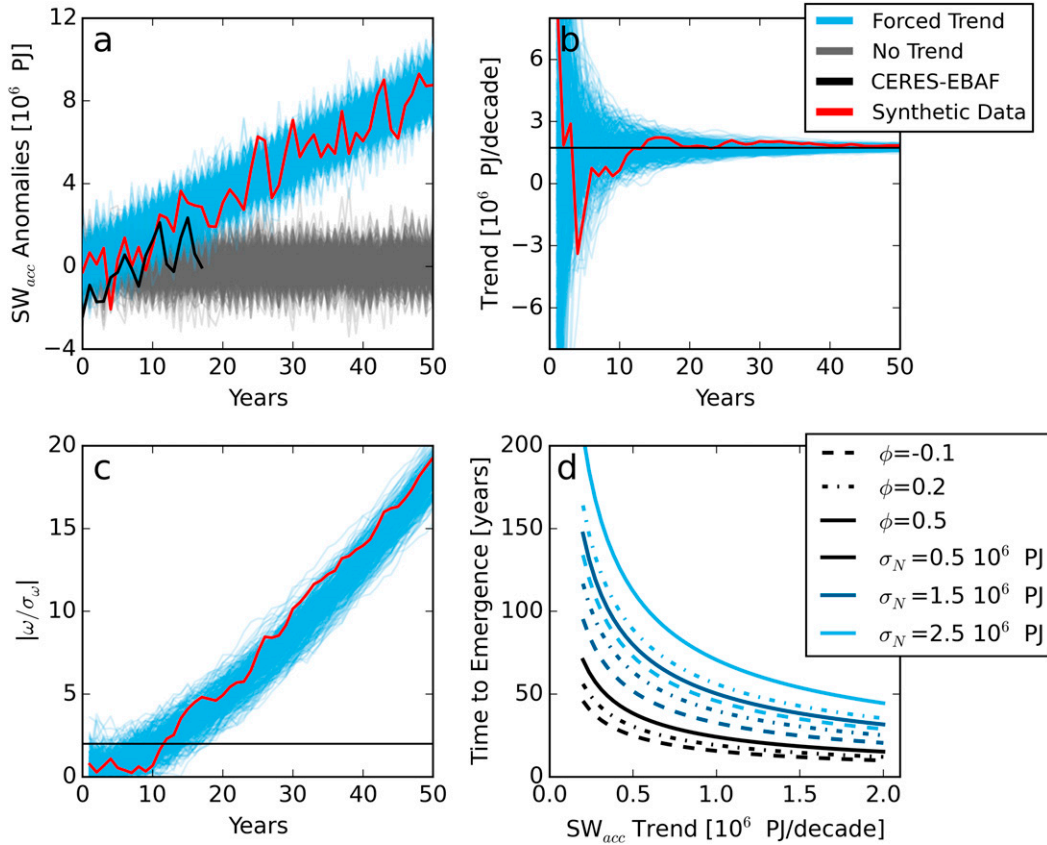
FIG. 2. Trend detection using synthetic time series of surface clear-sky (SFC$_{clr}$) accumulated shortwave (SW$_{acc}$) over the Arctic from CERES-EBAF. (a) Synthetic time series (gray) are generated based on the variance and lag-1 autocorrelation of the detrended CERES observations, shown in black. A linear trend based on the CERES record is added to time series to generate the ensemble shown in light blue. A single realization from the resulting ensemble is highlighted in red. (b) For each synthetic time series, the linear trend is calculated from subsets of time periods increasing in length, e.g., [0, 1], [0, 2], ... , [0, T], where T is the full length of the time series. Trends calculated over the red time series in (a) are again highlighted. Initially trends can vary greatly, oscillating between positive and negative values before leveling off around the "true" trend, given by the solid black line. (c) When the trend is at least 2 times as large as the uncertainty, shown as the solid black line at $|\hat{\omega}/\sigma_{\hat{\omega}}| = 2$ for the 95% confidence level, it is deemed to have "emerged." (d) Theoretical values of time to emergence (TTE) are shown with ranges of variability σ_N, lag-1 autocorrelation ϕ, and trend found in models and observations.

that the noise can be represented by an AR(1) process that is stationary. Many monthly time series in the Arctic do not meet these requirements, including monthly sea ice, albedo, and absorbed shortwave, as the variance and/or trends differ significantly throughout the seasons. We therefore calculate the net SW energy absorbed over the melt season, March through September. These months account for 95% of incoming SW radiation in the Arctic (Cao et al. 2016). The *accumulated SW*, SW$_{acc}$, is found by calculating the net SW flux (SW$^{\downarrow}$ − SW$^{\uparrow}$) absorbed at each grid box multiplied by the area of its grid box, converting it to a measure of power. Further multiplying by the duration (in seconds) of each month yields an accumulated energy. This average net SW energy is then summed over the Arctic, again defined as the area north of the Arctic Circle, and summed over the melt season:

$$SW_{acc} = \sum_{m=3}^{9} \sum_{i,j} (SW^{\downarrow} - SW^{\uparrow})_{i,j} \times A_{i,j} \times t_m, \quad (3)$$

where $A_{i,j}$ is the area of grid box i, j and t_m is the seconds in each month m.

Accumulated SW is a fundamental driver of Arctic climate variability. It is the net amount of SW energy input into the Arctic system that can go to melting sea ice and snow or heating the surface. Accumulated SW also behaves as a stationary time series, once detrended, unlike many other variables in the Arctic. We calculate SW$_{acc}$ at the TOA with all-sky fluxes (TOA$_{all}$) and at the surface with clear-sky fluxes (SFC$_{clr}$). Using these two boundaries and conditions allows us to quantify the difference clouds make at the TOA as compared to the surface if there were no clouds. Anomalies of SW$_{acc}$ are shown in Fig. 3 for CMIP6 and observations. As seen
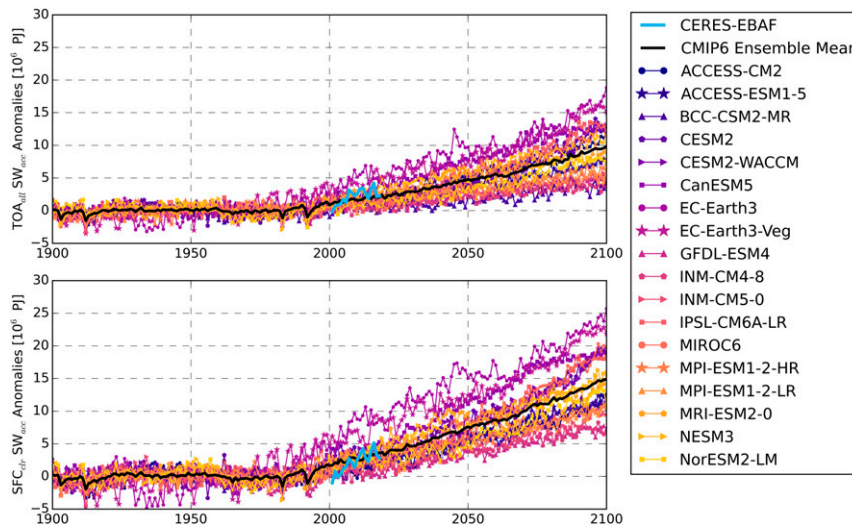
FIG. 3. Anomalies of SW_{acc} at (top) the top of the atmosphere with clouds (TOA_{all}) and (bottom) the surface without clouds (SFC_{clr}) in CMIP6 models and observations (CERES-EBAF). The ensemble mean from CMIP6 is shown in black. Anomalies for CMIP6 models are relative to 1900–99, and those from observations are calculated relative to 2001–18 but shifted to align with the CMIP6 base state (the CMIP6 ensemble mean from 2001 to 2018 is calculated and added to the CERES anomalies). For a given model, clear-sky SW_{acc} anomalies at the surface are greater than all-sky anomalies at the TOA. However, there are large differences between models in terms of both the magnitude and variability of anomalies.

with surface and TOA albedo anomalies (Fig. 1) clear-sky SW_{acc} increases faster than all-sky SW_{acc} at the TOA over the twenty-first century in all models.

Recall that the trend detection method assumes that the detrended anomalies can be represented by an AR(1) process. Increasing the time step (e.g., summing over the melt season) is intended to help meet this requirement, as mentioned in Gero and Turner (2011). In observations the noise has no significant autocorrelations at the 95% confidence level, which would suggest a white noise process, but this may be due to the short record length requiring large autocorrelations (≥ 0.47) to count as significant, shown in Fig. 4. In the majority of CMIP6 models, SW_{acc} noise appears as white or red noise over 1900–99, for example MRI-ESM2 in Fig. 4. According to Phojanamongkolkij et al. (2014), the method of Weatherhead et al. (1998) is more accurate for white or red noise scenarios when compared with other more general methods (e.g., Leroy et al. 2008) and they further suggest it is more appropriate for reflected SW irradiances.

Figure 2d shows the effect of trend, autocorrelation, and variance on TTE using values representative of observations and CMIP6 from Eq. (3) in Weatherhead et al. (1998). For smaller trends (less than approximately 0.1×10^6 PJ decade^{-1}) TTE is more sensitive to the trend than the noise or autocorrelation, but for SW_{acc} trends larger than approximately 0.2×10^6 PJ decade^{-1}, noise and autocorrelation can have a more significant impact. The magnitude of trends that TTE is sensitive to also depends on the level of noise. When a time series has greater variance it is more difficult to distinguish between what is just noise and what is indeed a consistent trend. For

example, the solid black line ($\phi = 0.5$ and $\sigma_N = 0.5 \times 10^6$ PJ) is flatter across trends ranging from 0.1×10^6 to 0.2×10^6 PJ decade^{-1} than the solid light blue line ($\phi = 0.5$ and $\sigma_N = 2.5 \times 10^6$ PJ) over the same range. Similarly, if a time series has high autocorrelation, what might appear to be a trend could simply be the propagation of an anomaly forward in time.

While the time series of annual SW_{acc} is a statistically convenient variable, using it instead of monthly averages shortens the data record length from monthly to annual reporting, from 12×18 data points to just 18. With such a short time period, it is reasonable to wonder if 18 years of satellite measurements are enough to observe a trend even with the rapid changes observed in the Arctic. The answer will be discussed in the following section.

3. Results and discussion

From the 18-yr CERES record, the trend in SW_{acc} at the surface without clouds, 1.7×10^6 PJ decade^{-1}, is statistically significant using the criteria $|\hat{\omega}/\sigma_{\hat{\omega}}| > 2$, but the trend in SW_{acc} at the TOA under all-sky conditions, 0.7×10^6 PJ decade^{-1}, is not. These trends and other statistics for CERES are listed in Table 2. The limited period of observations exhibits the striking feature that it is long enough to unambiguously detect anthropogenically forced clear-sky variations in absorbed SW radiation but not overall all-sky trends. If the TOA_{all} trend calculated over 2001–18 continues into the future, we find that it would take an average of 22 years for it to emerge above interannual variability. This extrapolation of the observed TOA_{all} SW_{acc} trend into
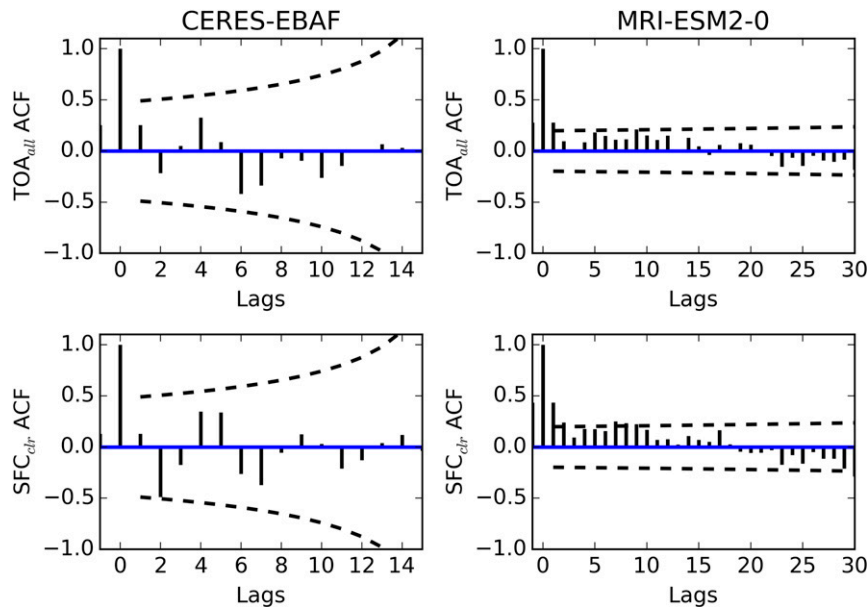
FIG. 4. Autocorrelation functions (ACF) for SW_{acc} anomalies at (top) TOA_{all} and (bottom) SFC_{clr} in (left) observations (CERES-EBAF) and (right) a typical climate model, MRI-ESM2. No autocorrelations are significant at any lags (95% confidence interval are shown as the dashed line); however, this may be due in part to the short record (18 years). When ACF are calculated over longer time periods in CMIP6 models, shown here for 1900–99, SW_{acc} anomalies usually appear as red or white noise.

the future to derive a hypothetical observational TTE is intended to suggest an approximate length of observational record where we might anticipate observing a significant measured trend; it is not an exact prediction of when the trend will emerge. This hypothetical TOA_{all} TTE (TTE_{all}) is nearly twice as long as that for SFC_{clr} found using a synthetic ensemble (12 years). The difference in observational TTE with and without clouds stems from the fact that the measured SFC_{clr} trend is more than twice as large as that of TOA_{all}, consistent with Sledd and L'Ecuyer (2019), while the noise and autocorrelations are similar (Table 2).

We can compare the results of calculating TTE from observations and models. Figure 5a shows the mean TTE from synthetic ensembles derived from CMIP6 models only using the variance and autocorrelation over 2001–18 forced with the trend evaluated from 2001 to 2100 for SSP245 and SSP585. Mean TTE from Fig. 5a are listed in Table 3. Across CMIP6, models predict the SW_{acc} trends

emerging within 8–35 years without clouds at the surface and 8–39 years with clouds at the TOA. The range of mean SFC_{clr} TTE (TTE_{clr}) in models is larger than the 2σ uncertainty of observations, 6–18 years, but more than half of the models predict mean TTE within 1 standard deviation of the observational TTE for at least one of the SSP. However, there are some differences between models and observations. Six models under SSP245 and 16 models under SSP585 predict mean TOA_{all} trends to have emerged within the observational record, contrary to our earlier findings. For SFC_{clr} trends, 17 models under SSP245 suggest a longer record would be needed for the trend emerge, reducing to only 11 models under SSP585, which is also in contrast to the observational results.

Different relationships between TTE_{all} and TTE_{clr} also emerge in Fig. 5a compared to TTE calculated using CERES. Under SSP245, half of the 18 models show clouds lengthening the TTE as in observations. Three models have mean TTE that are equal with and without clouds, and six models actually

TABLE 2. CERES-EBAF properties for all-sky top-of-atmosphere (TOA_{all}) and clear-sky surface (SFC_{clr}) accumulated shortwave (SW_{acc}). Noise, lag-1 autocorrelations, and trends are from 2001 to 2018. Mean time to emergence (TTE) is calculated from 300 synthetic time series using these statistics, with standard deviations given in parentheses.

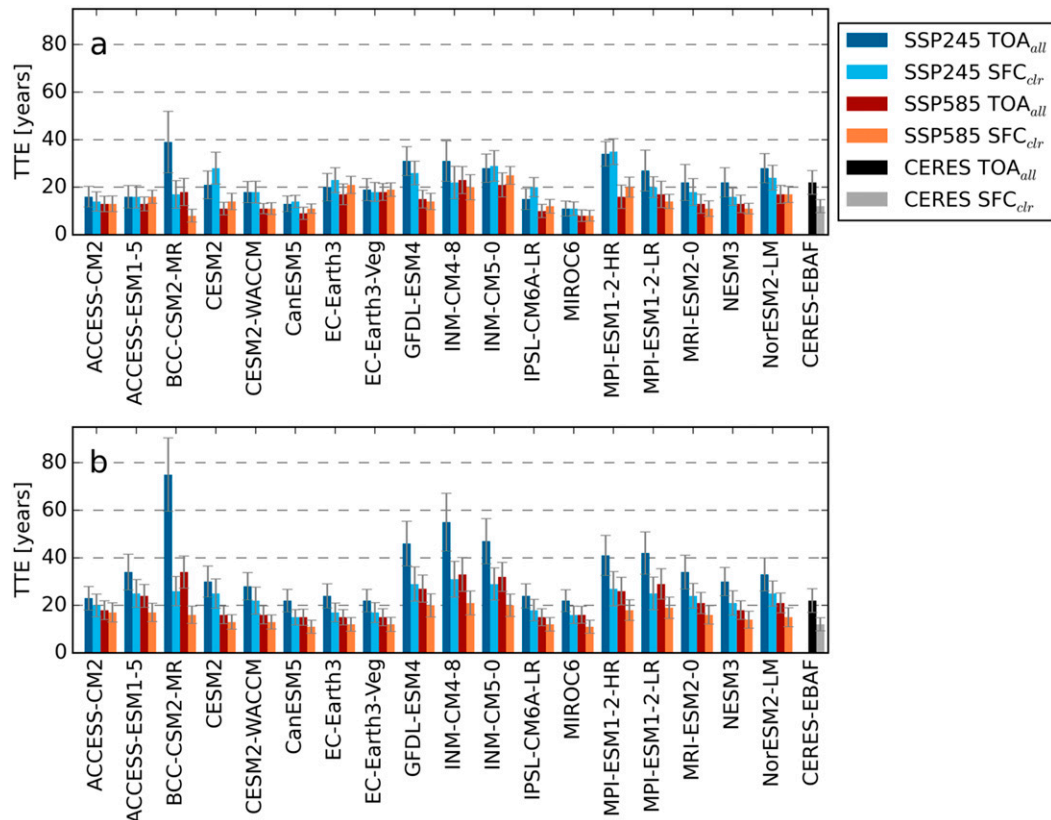|	Noise (10^6 PJ)	Autocorrelation	Trend (10^6 PJ decade^{-1})	TTE (yr)
TOA_{all}	0.77	0.29	0.72	22 (5)
SFC_{clr}	0.84	0.14	1.7	12 (3)

FIG. 5. (a) Mean TTE of SW$_{acc}$ trends from 300 synthetic time series based on CERES-EBAF observations and CMIP6 models. Variance and autocorrelation are calculated over 2001–18 and forced with trends over 2001–2100 for CMIP6 models and 2001–18 for CERES-EBAF. Error bars represent 1 standard deviation around the mean TTE. Two shared societal pathways (SSP) are shown: a "middle of the road" future (SSP245) and a "business as usual" future (SSP585). Observations suggest that trends in SFC$_{clr}$ SW$_{acc}$ have emerged in the 18-yr observational record whereas TOA$_{all}$ SW$_{acc}$ will require more years of observations to discern. (b) TTE calculated from synthetic time series with variability based on CERES-EBAF forced with trends from CMIP6 models used in (a). The difference between (a) and (b) shows the impacts of model internal variability on SW$_{acc}$ TTE. Values from bar plots are given in Tables 3 and 4.

show the opposite behavior of observations, with the all-sky SW$_{acc}$ trend emerging before the clear-sky trend. This result is unexpected based on our understanding of how clouds influence albedo in present-day observations, as shown in Fig. 1. When TTE is calculated using SSP585, only six models show clouds lengthening the TTE, three models show clouds having no effect on TTE, and nine models predict that clouds shorten the TTE.

To distinguish the influence of internal variability from modeled trends, we generate new synthetic time series that combine the statistical characteristics (σ and ϕ) from observations with trends from CMIP6 models calculated over the twenty-first century (2001–2100), shown in Fig. 5b and listed in Table 4. To disentangle biases in model internal variability versus the external forcing, we can compare TTE calculated solely from models to TTE calculated from observations forced by model trends. A significant difference between Figs. 5a and 5b is the impact of clouds on TTE magnitude. Unlike in Fig. 5a, clouds always increase

the TTE in Fig. 5b, consistent with observations, since in all models the SFC$_{clr}$ trend is larger than the TOA$_{all}$ trend. Biases in model noise and autocorrelations therefore must be a significant driver of why clouds shorten TTE in some models.

Figure 5b further suggests that few models capture the difference between TOA$_{all}$ and SFC$_{clr}$ trends. Under either SSP, nine of the 18 models predict TTE$_{clr}$ within one standard deviation of observations. Of these models, all but one (NorESM2-LM) predict that the TOA$_{all}$ trend should have emerged within the CERES record, which we do not observe. This is to say models may capture trends at one boundary but rarely both. Although we cannot know in the present what the trend in TOA$_{all}$ SW$_{acc}$ will be over the coming decades, we can characterize its current behavior, and it seems that many models may not fully capture the impact of clouds on SW$_{acc}$ in the Arctic.

The remainder of this study investigates how the statistical properties of SW$_{acc}$ affect TTE, what physically drives those

TABLE 3. TTE from 300 synthetic time series based on models only with noise and autocorrelation calculated from 2001 to 2018 forced with trends from 2001 to 2100. Standard deviations are given in parentheses.

	TOA$_{all}$ TTE (yr)		SFC$_{clr}$ TTE (yr)	
	SSP245	SSP585	SSP245	SSP585
ACCESS-CM2	16 (5)	13 (5)	14 (5)	13 (5)
ACCESS-ESM1.5	16 (7)	13 (8)	16 (6)	16 (6)
BCC-CSM2-MR	39 (15)	18 (15)	17 (6)	8 (6)
CESM2	21 (6)	11 (6)	28 (6)	14 (6)
CESM2(WACCM)	18 (6)	11 (6)	18 (6)	11 (6)
CanESM5	13 (5)	9 (5)	14 (3)	11 (3)
EC-Earth3	20 (5)	17 (5)	23 (4)	21 (4)
EC-Earth3-Veg	19 (5)	18 (5)	18 (4)	19 (4)
GFDL-ESM4	31 (9)	15 (9)	26 (7)	14 (7)
INM-CM4.8	31 (12)	23 (12)	22 (7)	20 (7)
INM-CM5.0	28 (9)	21 (9)	29 (7)	25 (7)
IPSL-CM6A-LR	15 (5)	10 (5)	20 (5)	12 (4)
MIROC6	11 (5)	8 (5)	11 (4)	8 (4)
MPI-ESM1.2-LR	34 (8)	16 (8)	35 (7)	20 (7)
MPI-ESM1.2-HR	27 (9)	17 (9)	20 (7)	14 (7)
MRI-ESM2	22 (7)	13 (7)	18 (5)	11 (5)
NESM3	22 (6)	13 (6)	16 (5)	11 (5)
NorESM2-LM	28 (7)	17 (7)	24 (5)	17 (5)

TABLE 4. TTE from 300 synthetic time series based on noise and autocorrelation from observations (CERES-EBAF) forced with trends from CMIP6 models over 2001–2100. Standard deviations are given in parentheses.

	TOA$_{all}$ TTE (yr)		SFC$_{clr}$ TTE (yr)	
	SSP245	SSP585	SSP245	SSP585
ACCESS-CM2	23 (5)	18 (5)	20 (5)	17 (5)
ACCESS-ESM1.5	34 (8)	24 (7)	25 (6)	17 (6)
BCC-CSM2-MR	75 (15)	34 (15)	26 (6)	16 (6)
CESM2	30 (6)	16 (6)	25 (6)	13 (6)
CESM2(WACCM)	28 (6)	16 (6)	22 (6)	13 (6)
CanESM5	22 (5)	15 (5)	15 (3)	11 (3)
EC-Earth3	24 (5)	15 (5)	17 (4)	12 (4)
EC-Earth3-Veg	22 (5)	15 (5)	17 (4)	12 (4)
GFDL-ESM4	46 (9)	27 (9)	29 (7)	20 (7)
INM-CM4.8	55 (12)	33 (12)	31 (7)	21 (7)
INM-CM5.0	47 (9)	32 (9)	29 (7)	20 (7)
IPSL-CM6A-LR	24 (5)	15 (5)	18 (4)	12 (4)
MIROC6	22 (5)	16 (5)	16 (4)	11 (4)
MPI-ESM1.2-HR	41 (8)	26 (8)	27 (7)	18 (7)
MPI-ESM1.2-LR	42 (9)	29 (9)	25 (7)	19 (7)
MRI-ESM2	34 (7)	21 (7)	24 (5)	16 (5)
NESM3	30 (6)	18 (6)	21 (5)	14 (5)
NorESM2-LM	33 (7)	21 (7)	25 (5)	15 (5)

properties, and why some models show behavior that is different than observations in regard to clouds lengthening TTE.

a. A signal-to-noise problem

In this section we assess the relative importance of SW$_{acc}$ trend, autocorrelation, and variability on TTE across climate models, beginning with how these statistics themselves can vary between distinct epochs within an individual model. While the observational record provides a limited number of years from which to calculate these statistics, that is not a limitation when using climate models. With the longer time series available from CMIP6 the influence of using different time periods on estimated TTE can be investigated, with the results being model-dependent. Using synthetic ensembles created by varying the starting year and length of time used to calculate the noise and autocorrelation (1983–2000, 1983–2018, 2001–18, and 2001–36) we find that only 7 and 6 of the 18 models generate mean TTE for TOA$_{all}$ trends and SFC$_{clr}$, respectively, within 1 standard deviation of each other regardless of which time period is used to generate the synthetic time series. The distinct behaviors of different models are exemplified by EC-Earth3 in Fig. 6, which exhibits a tightly constrained TTE, and GFDL-ESM4 where TTE can more than double across the range of time periods explored (plots for all models are provided in Fig. S1 of the online supplemental material). In all cases, trends are held constant for each model computed from either 1983 or 2001 through 2100.

For models where TTE varies markedly with epoch, the noise and autocorrelation are more sensitive to the time period than the trend is. Furthermore, noise and autocorrelation seem to be more sensitive to which epoch is used

rather than the length of the time period analyzed. For example, noise and autocorrelation in GFDL-ESM4 are relatively low during 2001–18 and 2001–36, whereas they increase during time periods that start in 1983 (1983–2000 and 1983–18).[1] On the other hand, trends in SW$_{acc}$ are fairly constant regardless of the time period for all models when determined over the twenty-first century. The consistency is likely due, in part, to the fact that the trend is measured over many decades, regardless of the starting year. This supports the assertion that we are testing for a consistent and measurable trend due to the external forcing. However, we note that if trends are calculated over shorter time periods, such as over 2001–18 to compare with our observational record, they are often not representative of the true forcing and are in fact occasionally negative (not shown). While only four different time periods are shown in Fig. 6, the same conclusions are drawn when more time periods are tested.

In the remaining analysis, we adopt the synthetic ensembles Fig. 5a is based on, where 2001–18 is used to calculate the

---

[1] The changes in measured SW$_{acc}$ variability may be due to the eruption of Mount Pinatubo in 1991, which caused a decrease in SW$_{acc}$. For models with relatively low variability, this decrease in SW$_{acc}$ would appear as large and would increase the variance for time periods including 1991 as compared with time periods without it. For models with relatively large SW$_{acc}$ variability, the decrease in SW$_{acc}$ resulting from the eruption of Mount Pinatubo would not be atypical and therefore would have a minimal impact on the measured variability.
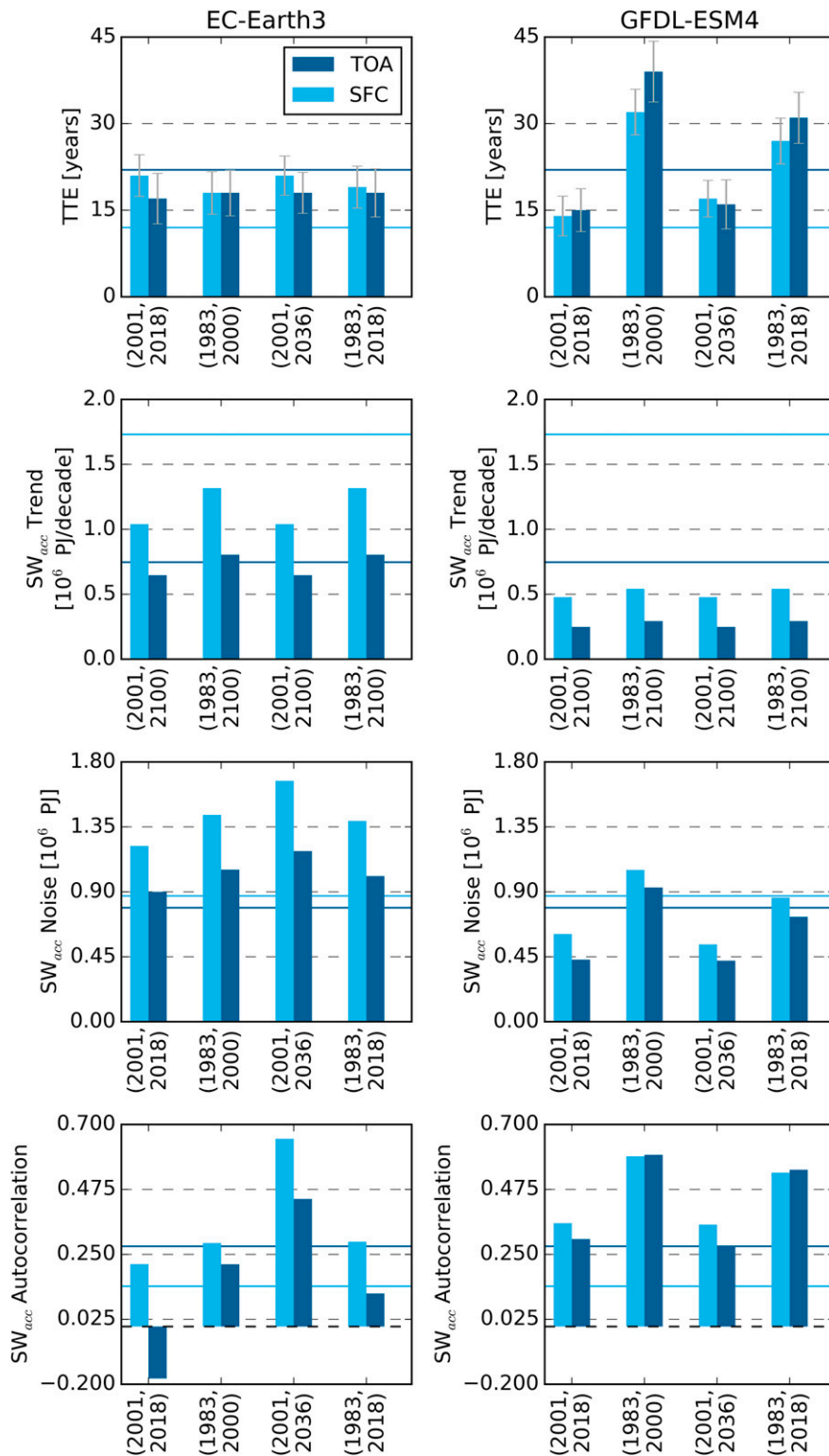
FIG. 6. TTE and statistical properties of TOA$_{all}$ and SFC$_{clr}$ SW$_{acc}$ used to calculate TTE from four different time periods. Solid lines represent values from CERES-EBAF. (left) TTE derived from EC-Earth3 is generally independent of the time period used to calculate it despite large variations in SW$_{acc}$ lag-1 autocorrelation. (right) TTE from GFDL-ESM4 vary by more than a factor of 2 between time periods. This variability is mostly due to differences in noise and autocorrelation as the SW$_{acc}$ trends are fairly consistent, regardless of the starting year. Although only time periods from SSP245 are shown, the results are consistent when using SSP585.
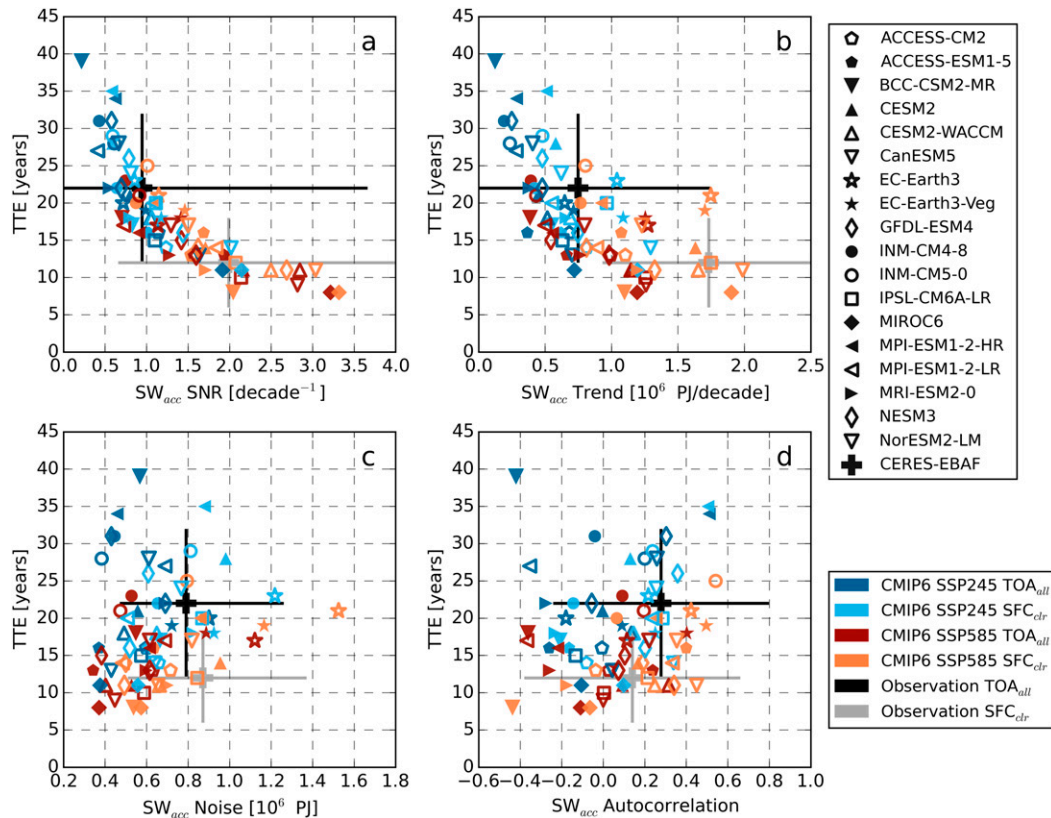
FIG. 7. Mean TTE and SW_{acc} statistical properties from 2001 to 2018 (noise and autocorrelation) and from 2001 to 2100 (trend) in CERES-EBAF and CMIP6. Error bars represent the 2σ range of uncertainty in observations. The SNR has the strongest relationship to TTE as it represents the strength of the trend against the variability, both with clouds at the top of the atmosphere (TOA_{all}) and without clouds at the surface (SFC_{clr}). Clouds reduce the magnitude of SW_{acc} trends, and sometimes the noise, within a given model. In observations, clouds significantly reduce the SNR, but for most models in CMIP6 they only have a moderate effect on SNR.

variance and autocorrelation and 2001–2100 is used to calculate trends. While the relationships between TTE and environmental factors discussed later are robust regardless of the chosen time periods, this choice of years allows a more consistent comparison with observations. Even in this one time period there are large intermodel differences in SW_{acc} forced trends and internal variability, shown in Fig. 7. Trends in SW_{acc} vary by an order of magnitude under SSP585 both with and without clouds and under SSP245 without clouds. Internal variability also varies significantly, doubling or even quadrupling across models, depending on the boundary and SSP. Seven of the models have variances within observational uncertainty for all boundaries and SSPs (using an F test with 95% confidence). Twice as many models (eight) differ significantly from observations for TOA_{all} than for SFC_{clr} (four). While models disagree on the sign of SW_{acc} autocorrelation, most fall within the 2σ range of uncertainty for the observational values.

These intermodel differences in SW_{acc} trend, autocorrelation, and variability in turn lead to differences in TTE. Mathematically, the main influence on TTE is the ratio of the forced SW_{acc} trend to the internal variability, that is, the

climate signal-to-noise ratio (SNR), shown in Fig. 7a. The SNR captures the primary question of TTE: when does a trend rise above the noise? Larger trends or smaller variability can increase SNR and reduce the TTE, but neither the trend (Fig. 7b) nor noise (Fig. 7c) alone is as strongly correlated to TTE as their ratio, both with and without clouds. Across models the trend has a greater impact on TTE than noise because it can vary by an order of magnitude while the noise varies by a factor of 4. Overall, the autocorrelation is weakly related to the TTE, despite ranging from positive to negative (Fig. 7d).

For a given model, the greatest differences between SSPs are in the strength of the forced SW_{acc} trends and the resulting SNR. As previously mentioned, SSP585 shows stronger trends in SW_{acc} than in SSP245, and therefore shorter TTE. Models with smaller trends than observations (indicated by plus signs in Fig. 7) often have longer TTE, and vice versa. Such is the case under SSP245 where SFC_{clr} trends (light blue) are underestimated in Fig. 7b. The inverse may be true for TOA_{all} trends (dark red) under SSP585, but it is uncertain given that the TOA_{all} trend has not emerged in the observations. Because of the different trend magnitudes,
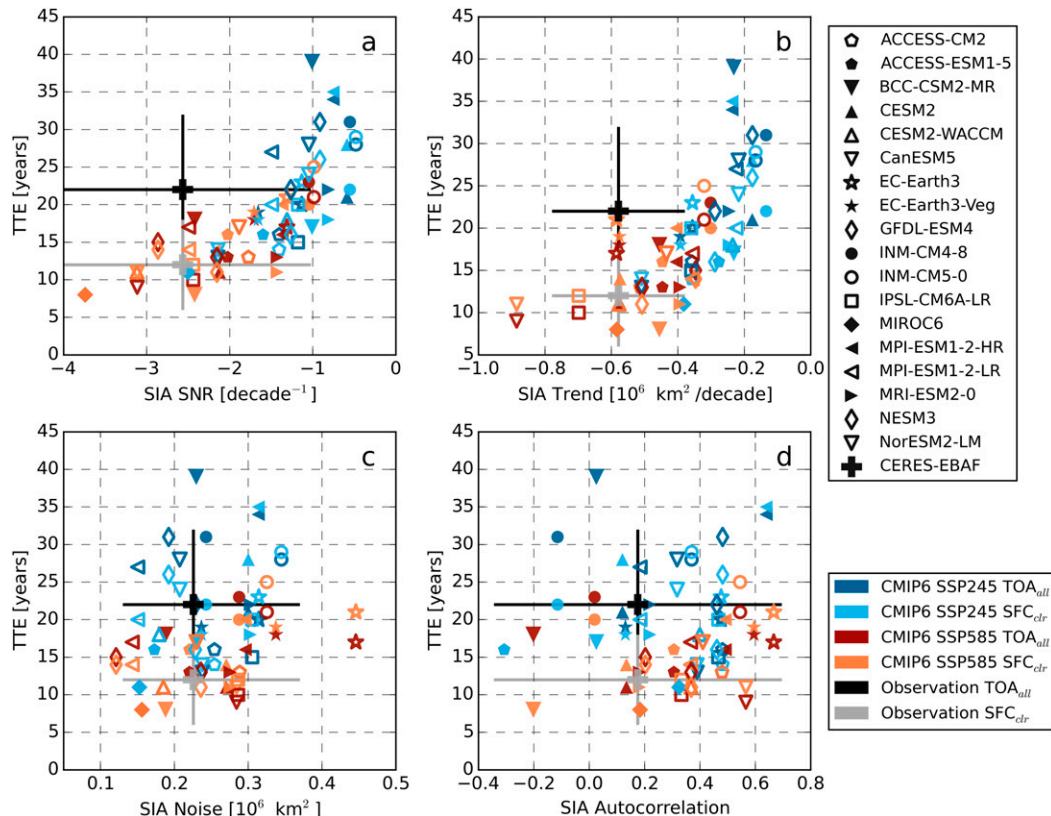
FIG. 8. Relationship between mean TTE for SW_{acc} and the statistical properties of sea ice area (SIA) averaged over the melt season (March–September) from 2001 to 2018 (noise and autocorrelation) and from 2001 to 2100 (trend). Error bars represent the 2σ range of uncertainty in observations. The greater the SIA decline is, the faster the SW_{acc} trend emerges, regardless of cloud cover. The SIA trend and SNR both impact SW_{acc} at SFC_{clr} and TOA_{all}. SIA noise is related to SFC_{clr} TTE but has a minimal influence on TOA_{all} TTE.

under SSP245 the SW_{acc} trend is a stronger predictor of TTE than noise because TTE is more sensitive to trend at these lower magnitudes, whereas noise and autocorrelation influence TTE more under SSP585, consistent with our discussion of theoretical TTE with Fig. 2d in section 3. Both SSPs have similar ranges of noise and autocorrelation across models, which is consistent with the SSPs not diverging until 2015. While the full range of SW_{acc} variability encompasses the observations in Fig. 7c, more models underestimate the observed variability in SW_{acc}, particularly at the TOA with clouds.

Differences between TOA_{all} and SFC_{clr} SW_{acc} behavior are fairly consistent across SSPs as well. As mentioned previously, clouds dampen the SW_{acc} trend at the TOA but not at the surface, and in models clouds also appear to reduce the variance of SW_{acc}. This impact has a few consequences. First, it means that trends are more linearly related to TTE for TOA_{all}, especially for SSP245 (dark blue in Fig. 7b), whereas SFC_{clr} noise and autocorrelation have stronger relationships to TTE than TOA_{all}, more notably for SSP585 (orange in Figs. 7c,d). Because clouds both dampen the signal and noise in models, the SNR are similar for SFC_{clr} and TOA_{all}.

Not all of these impacts of clouds are seen in observations, though. In observations, clouds reduce the measured SW_{acc} trends by more than a factor of 2 (black vs gray plus signs in Fig. 7b). Clouds have only a small impact on the noise and autocorrelation, so they ultimately reduce the SNR by a factor of 2 between SF_{clr} and TOA_{all} as well. This impact of clouds is not always found in CMIP6 models despite the observational values being within the ensemble ranges.

b. Impact of sea ice on TTE

Sea ice influences numerous aspects of the Arctic climate, including SW_{acc}. The more rapidly and consistently sea ice disappears, the faster the SW_{acc} trend emerges, as shown in Fig. 8. Trends in sea ice area (SIA) over the twenty-first century strongly influence the TTE both with and without clouds and under SSP245 and SSP585 (Fig. 8b). The SNR of SIA is also correlated with TTE (Fig. 8a), mostly due to the impact of SIA decline and to a lesser extent the variability of SIA (Fig. 8c). We find that SIA autocorrelation has little impact on SW_{acc} TTE (Fig. 8d), likely because persistence of sea ice anomalies tends not to extend beyond a year (Blanchard-Wrigglesworth et al. 2011).

The importance of SIA on SW_{acc} is physically consistent with our understanding of the Arctic energy budget and the ice albedo feedback. However, there are some subtleties that are smoothed over when using SW_{acc} and SIA. SIA and SW_{acc} encompass the entire melt season, which removes some of the strong differences between March and September. While sea ice decline is largest in the autumn when it reaches its minimum, incoming SW peaks in June. Sea ice in midsummer, therefore, has a larger impact on the Arctic albedo and absorbed SW. Relating SIA to SW_{acc} also ignores changes in sea ice albedo throughout the melt seasons, which can be significant when melt ponds form (Perovich et al. 2002).

While SIA strongly influences SW_{acc} under both SSPs, there are some slight differences between the two forcing pathways that are highlighted in Fig. 8. As would be expected, SIA trends are larger under SSP585 due to increased GHG emissions and warming for individual models. SIA observations calculated over 2001–18 are closer to values from SSP585, but there is some overlap in the rate of SIA decline between SSPs when looking at the full CMIP6 ensemble. SIA noise also seems to influence TTE more in SSP585 than SSP245, as was the case for SW_{acc} in Fig. 7b. This is likely due to the greater trends in SIA pushing TTE into a regime where noise and autocorrelation can have greater impacts, as discussed with theoretical SW_{acc} TTE in Fig. 2d.

c. Inconsistent cloud impacts on TTE

Figure 8 further suggests that model cloud biases may influence their predictions of the emergence of forced variations in all-sky SW_{acc}. Recently observed trends in SIA fall within the envelope of behavior predicted by the CMIP6 ensemble, and the relationship between TTE_{clr} and SIA seen in observations is represented in models. All models, however, underestimate the relationship between TTE_{all} and SIA trend and SNR. For example, while EC-Earth3 produces a similar trend in SIA to observations, the TTE_{clr} from EC-Earth3 actually resembles the TTE_{all} projected from observations (Fig. 7b). The TTE_{all} is 7 yr shorter in EC-Earth3 than observations and is actually shorter than SFC_{clr}, while observations suggest that clouds lengthen the TTE. This is a common bias in which many models seem to struggle predicting the impact of clouds on forced climate trends.

We now turn to the question of why clouds shorten the TTE in some models, contrary to observations and physical intuition. In observations, clouds increase the TTE from SFC_{clr} to TOA_{all} because the SW_{acc} trend is smaller with clouds while the noise and autocorrelations are similar (Table 2). Admittedly, the TOA_{all} trend and therefore TTE are uncertain in observations, but we can find the minimum possible difference in TTE_{all} and TTE_{clr}. If one more year of observations proved the TOA_{all} trend significant, for example $TTE_{all} = 18 + 1$, the minimum ratio of TTE_{all} to TTE_{clr} would be $19/12 = 1.6$—over a 50% increase. This cloud masking effect has been documented in several other studies and means that the SFC_{clr} SNR is larger than that of TOA_{all}. Many models do not reproduce these relationships, though. In Fig. 9, for example, only one model, BCC-CSM2-MR, predicts a TTE_{all} to TTE_{clr} ratio larger than

observations or even the minimum ratio of TOA_{all} to SFC_{clr}, shown with the shaded region in Fig. 9.

Because SW_{acc} SNR is strongly correlated with TTE, its ratio of TOA_{all} to SFC_{clr} is also strongly correlated to the ratio of TTE, shown in Fig. 9a. Above an SNR of approximately 0.8, the TOA_{all} trend may emerge before the SFC_{clr}. In some models, clouds even cause the SNR to be higher at the TOA relative to the surface ($TOA_{all}/SFC_{clr} > 1$), which is opposite to observations. While the SNR is dependent on the ratio of trends with and without clouds, clouds dampen the SW_{acc} signal in all models (Fig. 9b). For the TOA_{all} trend to emerge first, clouds must also appreciably dampen the TOA_{all} variability (Fig. 9c).

For any given model, the ratios of TTE and SW_{acc} properties do not vary appreciably between SSPs. While SW_{acc} trends can differ by an order of magnitude between SSP245 and SSP585 in Fig. 7b, the ratios are never more than 2 times as large in Fig. 9b. For example, the ratio of trends in BCC-CSM2-MR (filled upside-down triangles) only vary from 0.2 (SSP 245; blue) to 3.5 (SSP585; orange), with most other models varying even less between SSPs. That is to say, the impact of clouds on SW_{acc} is likely due to inherent model physics rather than uncertainty from external forcings.

So how do clouds influence the climate SNR and resulting TTE? Over the Arctic, models vary widely in their predicted cloud fraction (CF) responses over the melt season with some showing increases, others showing decreases, and some having no change (Fig. 10). The sign of modeled CF trend plays a significant role in defining the how surface albedo changes manifest themselves in changes in absorbed SW radiation at the TOA. Models that predict decreasing CF predict stronger TOA_{all} SW_{acc} trends, stronger TOA_{all} SNR, and shorter TTE_{all} than exist at the surface, indicative of a cloud feedback that amplifies the influence of sea ice on absorbed shortwave radiation. This relationship is stronger under SSP585 as the magnitude of CF trends increases with climate forcing for any given model. Reduced cloud cover in models can reduce the planetary albedo in a few ways. Clouds directly reflect incoming SW at the TOA, so reduced cloud cover results in an increase of insolation at the surface. In addition, the presence of fewer clouds means that changes in the surface albedo are more directly seen from space, amplifying the albedo impact of sea ice loss. Models with negative CF trend, therefore, have SW_{acc} trends that are closer in magnitude with and without clouds at the TOA and surface in Fig. 10c. At the opposite end of the spectrum, the only model that shows a TTE ratio greater than observations, BCC-CSM2-MR, also has the largest positive trend in CF and greatest difference between TOA_{all} and SFC_{clr} SW_{acc} trends.

Cloud fraction alone does not, however, explain all of the differences between TOA_{all} and SFC_{clr} SW_{acc} in Fig. 10. Mean CF over 2001–18 has no impact on the ratio between TTE_{all} and TTE_{clr}, noise, or autocorrelation during the time period (not shown). Furthermore, the radiative impacts of clouds also depend on the microphysical properties. In particular, cloud phase can have a substantial impact on SW
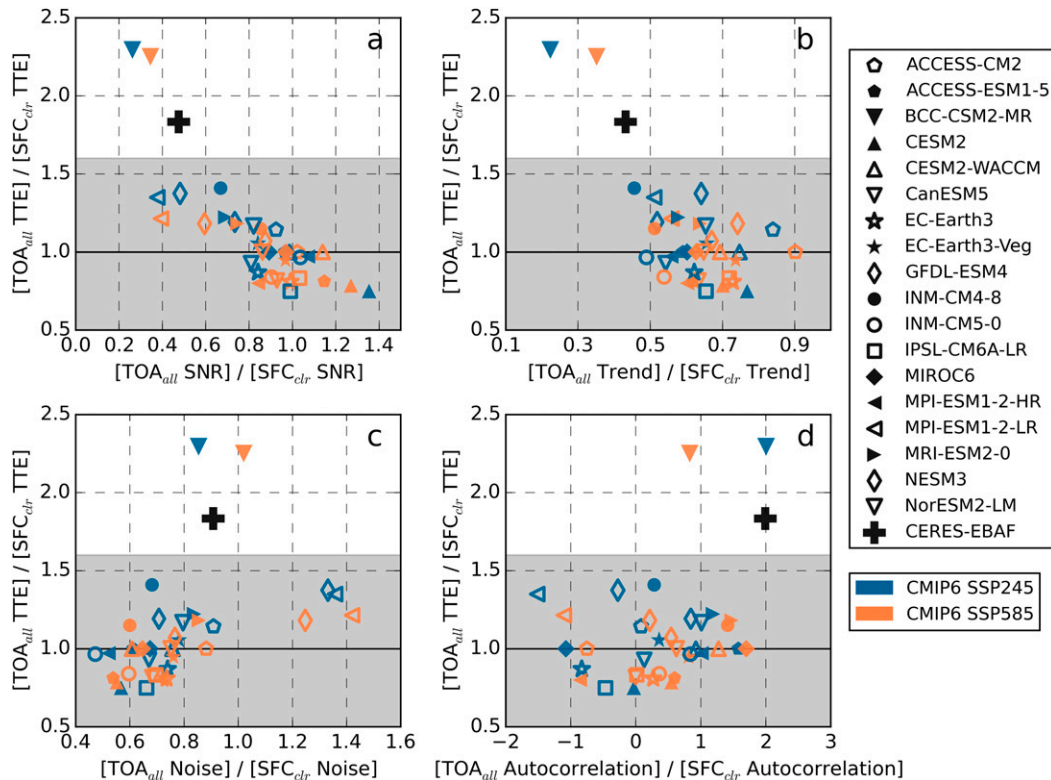
FIG. 9. Dependence of the ratio of TOA$_{all}$ to SFC$_{clr}$ SW$_{acc}$ TTE on SW$_{acc}$ statistical properties. The shaded region represents TTE ratios below the minimum ratio if one more year of observations proved the TOA$_{all}$ trend to be significant. The relative strength of the SNR with and without clouds is negatively related to the relative length of TTE. When the TOA and surface SW$_{acc}$ trends are similar, the TOA SW$_{acc}$ trend may emerge sooner if the natural variability at the surface is larger than that at TOA. This relationship holds for both SSPs. Most models underestimate the influence that clouds damping the SW$_{acc}$ trend and SNR has on the difference in TTE.

radiative forcing (Cesana et al. 2012; McIlhattan et al. 2017). We suspect discrepancies in cloud phase between models could further explain differences in noise between TOA$_{all}$ and SFC$_{clr}$ SW$_{acc}$ given that such differences in cloud phase have explained past biases in model SW cloud radiative forcing in the Arctic (Gorodetskaya et al. 2008) and can further impact the global mean cloud feedback (Zelinka et al. 2020). While relevant, a detailed analysis linking cloud phase and differences in TOA$_{all}$ and SFC$_{clr}$ SW$_{acc}$ would require data with higher temporal resolution than are currently available through CMIP6 for all but a few of the models used in this work.

d. SW$_{acc}$ as a proxy for Arctic and global change

As noted in the introduction, the amount of solar radiation absorbed in the Arctic, SW$_{acc}$, is a fundamental driver of Arctic climate. This relationship is shown more directly in Fig. 11a that quantifies the relationship between TTE$_{all}$ and Arctic warming over the twenty-first century in the CMIP6 models. While the calculation of TTE$_{all}$ is independent of temperature trends, Fig. 11a shows that it is strongly correlated with the projected change in annual average surface temperature in

Arctic (ΔT; defined as temperature averaged over 2081–2100 minus temperature averaged over 2001–18). This demonstrates very clearly that there is a connection between greater Arctic warming, increasing SW$_{acc}$, and increased sea ice loss. Models with stronger ice-albedo feedbacks have warmer oceans that promote more rapid sea ice melt, stronger increases in SW$_{acc}$ (i.e., shorter TTE), and, in turn, more ocean warming. Yet while TTE$_{all}$ appears related to both Arctic and global warming, it has essentially no relationship to Arctic amplification (AA), the relative magnitude of Arctic warming to global warming. In Fig. 11c a wide range of TTE$_{all}$ (10–40 years) cluster near AA values around 2.5.

While this analysis does not reveal the precise nature of these processes or their timing (i.e., cause and effect), it suggests that TTE$_{all}$ could be a useful proxy for Arctic climate change for which we have a growing observational record. In addition, TTE$_{all}$ may be a good predictor of global temperature changes over the twenty-first century, particularly for the "business as usual" pathway, SSP585 (Fig. 11b). Changes in global mean surface temperature from 2001–18 to 2081–2100 decrease sharply with increasing TTE. This relationship suggests that the strength of Arctic SW$_{acc}$ trends, relative to
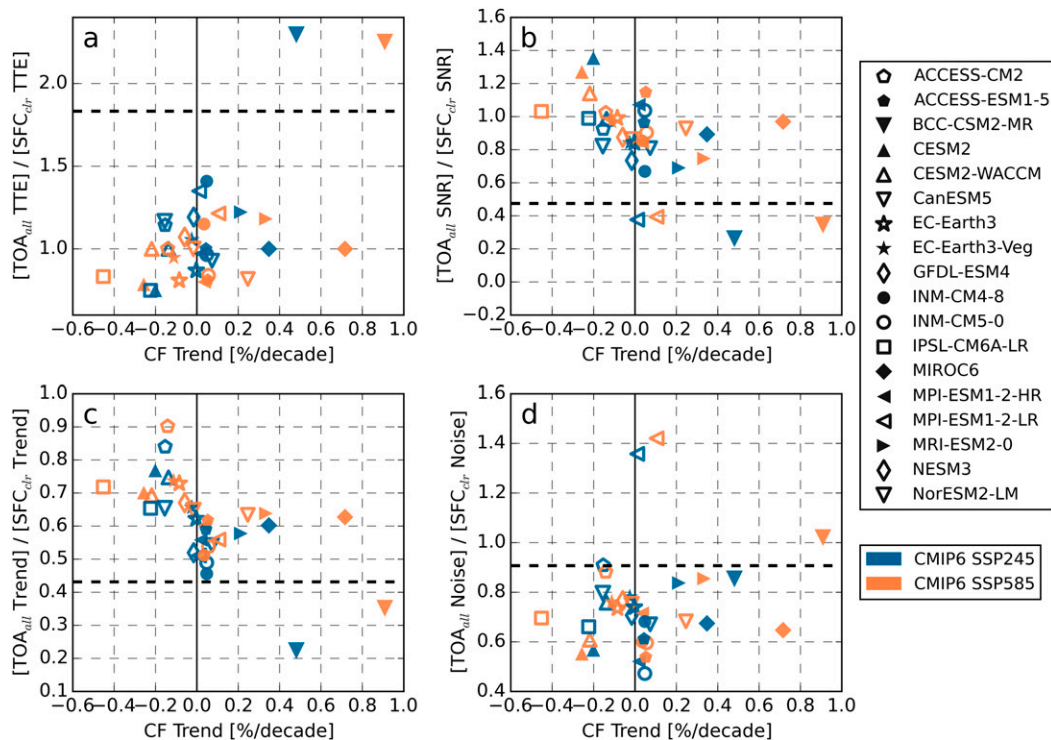
FIG. 10. Role of twenty-first-century cloud fraction (CF) trends in modulating the ratio of TOA_{all} to SFC_{clr} accumulated shortwave TTE. The atmosphere, and clouds in particular, account for much of the planetary albedo both globally and in the Arctic. Models that predict decreasing cloud cover over the twenty-first century amplify the effect of reduced surface albedo from sea ice on TOA SW_{acc} by both lowering the atmospheric contribution to the planetary albedo and revealing dark open ocean. This impact is linked to the relative strength of SW_{acc} trends and SNR with and without clouds in both SSPs.

interannual variability, may be a good observation-based proxy for both Arctic and global temperature change but not AA.

4. Conclusions

This work evaluates forced and natural variations in Arctic absorbed shortwave radiation in observations and GCMs to establish the time to emergence of trends and how they are influenced by clouds. We find that the observed trend in clear-sky SW_{acc} at the surface is significant at the 95% confidence level using only 18 years of satellite observations. Clouds reduce the SW_{acc} trend measured in observations by at least half at the TOA resulting in the conclusion that the current observational record is insufficient to confirm any forced trend in SW_{acc} relative to interannual variability.

The 18 CMIP6 models analyzed in this study exhibit large intermodel spread in both forced trends and internal variability: SW_{acc} trends vary by an order of magnitude and natural variability varies by up to a factor of 4. CMIP6 models further disagree on the effect of clouds on trends in SW_{acc}. While some predict that clouds increase TTE, consistent with observations, many fail to reproduce this fundamental feature in the CERES-EBAF record (Fig. 1), possibly as a result of cloud

feedbacks that artificially augment the SNR of surface albedo signatures at the TOA. The magnitude of TTE is largely driven by the decline of sea ice in models, as the statistical behavior of SIA largely determines those of SW_{acc} both with and without clouds. Trends in GCM cloud cover over the twenty-first century dictate whether or not clouds increase or decrease the time needed to detect a trend in SW_{acc}. Models that predict decreasing CF with Arctic warming predict stronger TOA_{all} SW_{acc} trends and shorter TTE_{all} than without clouds, but further work is needed to assess the role of cloud microphysical properties and phase in modulating SW_{acc} trends in the Arctic.

Accumulated SW radiation is linked to both Arctic and global temperature changes and shows potential as an observational metric of future Arctic climate change impacts. The results presented here suggest that the trend in TOA_{all} SW_{acc} may emerge from interannual variability in the next decade. Thus, the extended observation record provided by continued CERES measurements and the planned Earth Radiation Budget continuity mission, Libera, will, it is hoped, be of sufficient duration to determine the the TOA_{all} trend. In turn this would allow the identification of climate models that best capture the processes that govern this fundamental measure of Arctic climate. Deeper investigation into the sea ice and cloud trends in these models may improve understanding of these
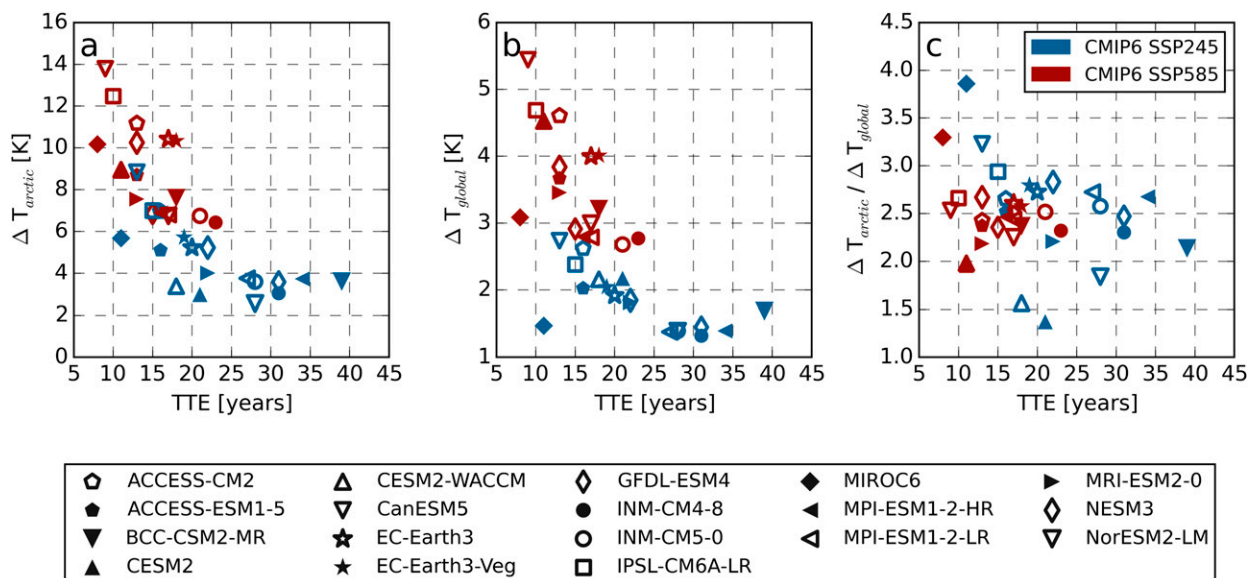
FIG. 11. Relationships between (a) Arctic warming, (b) global warming, and (c) Arctic amplification (AA) and TOA$_{all}$ TTE from CMIP6. Temperature changes ΔT are derived from the difference in annual average surface temperature of 2081–2100 relative to 2001–18. The time to emergence of all-sky absorbed SW radiation trends in the Arctic may be a good proxy for both Arctic and global temperature change in both warming pathways. Since sea ice loss drives much of the intermodel variability of TTE, models with more warming have quicker sea ice loss and lower TTE, as seen in (a). A similar relationship appears to hold for global temperature [in (b)] but not for AA [in (c)].

key drivers of Arctic climate and, possibly, provide a constraint on anticipated global temperature change.

Data availability statement. ArORIS is available online (http://www.cloudsat.cira.colostate.edu/community-products/arctic-observation-and-reanalysis-integrated-system). All data from CMIP6 are available from the ESGF (https://esgf-node.llnl.gov/projects/esgf-llnl/).

REFERENCES

Blanchard-Wrigglesworth, E., K. C. Armour, C. M. Bitz, and E. DeWeaver, 2011: Persistence and inherent predictability of Arctic sea ice in a GCM ensemble and observations. *J. Climate*, **24**, 231–250, https://doi.org/10.1175/2010JCLI3775.1.

Box, J. E., and Coauthors, 2019: Key indicators of Arctic climate change: 1971–2017. *Environ. Res. Lett.*, **14**, 045010, https://doi.org/10.1088/1748-9326/aafc1b.

Brodzik, M. J., and R. Armstrong, 2013: Northern Hemisphere EASE-grid 2.0 weekly snow cover and sea ice extent, version 4. NASA National Snow and Ice Data Center Distributed Active Archive Center, accessed 26 August 2019, https://doi.org/10.5067/P7O0HGJLYUQU.

Cao, Y., S. Liang, T. He, and X. Chen, 2016: Evaluation of four reanalysis surface albedo data sets in Arctic using a satellite product. *IEEE Geosci. Remote Sens. Lett.*, **13**, 384–388, https://doi.org/10.1109/LGRS.2016.2515159.

Carmack, E., and Coauthors, 2015: Toward quantifying the increasing role of oceanic heat in sea ice loss in the new Arctic. *Bull. Amer. Meteor. Soc.*, **96**, 2079–2105, https://doi.org/10.1175/BAMS-D-13-00177.1.

Cesana, G., J. Kay, H. Chepfer, J. English, and G. de Boer, 2012: Ubiquitous low-level liquid-containing Arctic clouds: New observations and climate model constraints from CALIPSO-GOCCP. *Geophys. Res. Lett.*, **39**, L053385, https://doi.org/10.1029/2012GL053385.

Chepfer, H., V. Noël, M. Chiriaco, B. Wielicki, D. Winker, N. Loeb, and R. Wood, 2018: The potential of a multidecade spaceborne lidar record to constrain cloud feedback. *J. Geophys. Res. Atmos.*, **123**, 5433–5454, https://doi.org/10.1002/2017JD027742.

Christensen, M. W., A. Behrangi, T. S. L'Ecuyer, N. B. Wood, M. D. Lebsock, and G. L. Stephens, 2016: Arctic observation and reanalysis integrated system: A new data product for validation and climate study. *Bull. Amer. Meteor. Soc.*, **97**, 907–916, https://doi.org/10.1175/BAMS-D-14-00273.1.

Comiso, J. C., 2002: A rapidly declining perennial sea ice cover in the Arctic. *Geophys. Res. Lett.*, **29**, 1956, https://doi.org/10.1029/2002GL015650.

——, C. L. Parkinson, R. Gersten, and L. Stock, 2008: Accelerated decline in the Arctic sea ice cover. *Geophys. Res. Lett.*, **35**, L01703, https://doi.org/10.1029/2007GL031972.

Curry, J. A., J. L. Schramm, and E. E. Ebert, 1995: Sea ice–albedo climate feedback mechanism. *J. Climate*, **8**, 240–247, https://doi.org/10.1175/1520-0442(1995)008<0240:SIACFM>2.0.CO;2.

Dolinar, E. K., X. Dong, B. Xi, J. H. Jiang, and H. Su, 2015: Evaluation of CMIP5 simulated clouds and TOA radiation budgets using NASA satellite observations. *Climate Dyn.*, **44**, 2229–2247, https://doi.org/10.1007/s00382-014-2158-9.

Donohoe, A., and D. S. Battisti, 2011: Atmospheric and surface contributions to planetary albedo. *J. Climate*, **24**, 4402–4418, https://doi.org/10.1175/2011JCLI3946.1.

Eyring, V., S. Bony, G. A. Meehl, C. A. Senior, B. Stevens, R. J. Stouffer, and K. E. Taylor, 2016: Overview of the Coupled Model Intercomparison Project Phase 6 (CMIP6) experimental design and organization. *Geosci. Model Dev.* **9**, 1937–1958, https://doi.org/10.5194/GMD-9-1937-2016.

Feldman, D. R., C. A. Algieri, W. D. Collins, Y. L. Roberts, and P. A. Pilewskie, 2011: Simulation studies for the detection of changes in broadband albedo and shortwave nadir reflectance spectra under a climate change scenario. *J. Geophys. Res.*, **116**, D10107, https://doi.org/10.1029/2010JD015350.

Gero, P. J., and D. D. Turner, 2011: Long-term trends in downwelling spectral infrared radiance over the U.S. southern Great Plains. *J. Climate*, **24**, 4831–4843, https://doi.org/10.1175/2011JCLI4210.1.

Gorodetskaya, I. V., M. A. Cane, L.-B. Tremblay, and A. Kaplan, 2006: The effects of sea-ice and land-snow concentrations on planetary albedo from the Earth Radiation Budget Experiment. *Atmos.–Ocean*, **44**, 195–205, https://doi.org/10.3137/ao.440206.

——, L.-B. Tremblay, B. Liepert, M. A. Cane, and R. I. Cullather, 2008: The influence of cloud and surface properties on the Arctic Ocean shortwave radiation budget in coupled models. *J. Climate*, **21**, 866–882, https://doi.org/10.1175/2007JCLI1614.1.

Hwang, J., Y.-S. Choi, W. Kim, H. Su, and J. H. Jiang, 2018: Observational estimation of radiative feedback to surface air temperature over northern high latitudes. *Climate Dyn.*, **50**, 615–628, https://doi.org/10.1007/s00382-017-3629-6.

Katlein, C., S. Hendricks, and J. Key, 2017: Brief communication: Antarctic sea ice gain does not compensate for increased solar absorption from Arctic ice loss. *Cryosphere Discuss.*, https://doi.org/10.5194/tc-2016-279.

Kato, S., N. G. Loeb, P. Minnis, J. A. Francis, T. P. Charlock, D. A. Rutan, E. E. Clothiaux, and S. Sun-Mack, 2006: Seasonal and interannual variations of top-of-atmosphere irradiance and cloud cover over polar regions derived from the CERES data set. *Geophys. Res. Lett.*, **33**, L19804, https://doi.org/10.1029/2006GL026685.

——, and Coauthors, 2018: Surface irradiances of edition 4.0 Clouds and the Earth's Radiant Energy System (CERES) Energy Balanced and Filled (EBAF) data product. *J. Climate*, **31**, 4501–4527, https://doi.org/10.1175/JCLI-D-17-0523.1.

Kay, J. E., and A. Gettelman, 2009: Cloud influence on and response to seasonal Arctic sea ice loss. *J. Geophys. Res.*, **114**, D18204, https://doi.org/10.1029/2009JD011773.

——, and T. L'Ecuyer, 2013: Observational constraints on Arctic Ocean clouds and radiative fluxes during the early 21st century. *J. Geophys. Res. Atmos.*, **118**, 7219–7236, https://doi.org/10.1002/jgrd.50489.

——, ——, H. Chepfer, N. Loeb, A. Morrison, and G. Cesana, 2016: Recent advances in Arctic cloud and climate research.

Curr. Climate Change Rep., **2**, 159–169, https://doi.org/10.1007/s40641-016-0051-9.

Leroy, S. S., J. G. Anderson, and G. Ohring, 2008: Climate signal detection times and constraints on climate benchmark accuracy requirements. *J. Climate*, **21**, 841–846, https://doi.org/10.1175/2007JCLI1946.1.

Li, J.-L., D. Waliser, G. Stephens, S. Lee, T. L'Ecuyer, S. Kato, N. Loeb, and H.-Y. Ma, 2013: Characterizing and understanding radiation budget biases in CMIP3/CMIP5 GCMs, contemporary GCM, and reanalysis. *J. Geophys. Res. Atmos.*, **118**, 8166–8184, https://doi.org/10.1002/jgrd.50378.

Lian, T., 2017: Uncertainty in detecting trend: A new criterion and its applications to global SST. *Climate Dyn.*, **49**, 2881–2893, https://doi.org/10.1007/s00382-016-3483-y.

Lindsay, R., and A. Schweiger, 2015: Arctic sea ice thickness loss determined using subsurface, aircraft, and satellite observations. *Cryosphere*, **9**, 269–283, https://doi.org/10.5194/tc-9-269-2015.

Loeb, N. G., and Coauthors, 2018: Clouds and the Earth's Radiant Energy System (CERES) Energy Balanced and Filled (EBAF) top-of-atmosphere (TOA) edition-4.0 data product. *J. Climate*, **31**, 895–918, https://doi.org/10.1175/JCLI-D-17-0208.1.

——, and Coauthors, 2020: Toward a consistent definition between satellite and model clear-sky radiative fluxes. *J. Climate*, **33**, 61–75, https://doi.org/10.1175/JCLI-D-19-0381.1.

McIlhattan, E. A., T. S. L'Ecuyer, and N. B. Miller, 2017: Observational evidence linking Arctic supercooled liquid cloud biases in CESM to snowfall processes. *J. Climate*, **30**, 4477–4495, https://doi.org/10.1175/JCLI-D-16-0666.1.

Morrison, A., J. E. Kay, H. Chepfer, R. Guzman, and V. Yettella, 2018: Isolating the liquid cloud response to recent Arctic sea ice variability using spaceborne lidar observations. *J. Geophys. Res. Atmos.*, **123**, 473–490, https://doi.org/10.1002/2017JD027248.

——, ——, W. Frey, H. Chepfer, and R. Guzman, 2019: Cloud response to Arctic sea ice loss and implications for future feedback in the CESM1 climate model. *J. Geophys. Res. Atmos.*, **124**, 1003–1020, https://doi.org/10.1029/2018JD029142.

Onarheim, I. H., and M. Årthun, 2017: Toward an ice-free Barents Sea. *Geophys. Res. Lett.*, **44**, 8387–8395, https://doi.org/10.1002/2017GL074304.

——, T. Eldevik, L. H. Smedsrud, and J. C. Stroeve, 2018: Seasonal and regional manifestation of Arctic sea ice loss. *J. Climate*, **31**, 4917–4932, https://doi.org/10.1175/JCLI-D-17-0427.1.

O'Neill, B. C., and Coauthors, 2016: The Scenario Model Intercomparison Project (ScenarioMIP) for CMIP6. *Geosci. Model Dev.*, **9**, 3461–3482, https://doi.org/10.5194/gmd-9-3461-2016.

Perovich, D., T. Grenfell, B. Light, and P. Hobbs, 2002: Seasonal evolution of the albedo of multiyear Arctic sea ice. *J. Geophys. Res.*, **107**, 8044, https://doi.org/10.1029/2000JC000438.

Phojanamongkolkij, N., S. Kato, B. A. Wielicki, P. C. Taylor, and M. G. Mlynczak, 2014: A comparison of climate signal trend detection uncertainty analysis methods. *J. Climate*, **27**, 3363–3376, https://doi.org/10.1175/JCLI-D-13-00400.1.

Pistone, K., I. Eisenman, and V. Ramanathan, 2014: Observational determination of albedo decrease caused by vanishing Arctic sea ice. *Proc. Natl. Acad. Sci. USA*, **111**, 3322–3326, https://doi.org/10.1073/pnas.1318201111.

Qu, X., and A. Hall, 2005: Surface contribution to planetary albedo variability in cryosphere regions. *J. Climate*, **18**, 5239–5252, https://doi.org/10.1175/JCLI3555.1.

Sedlar, J., and Coauthors, 2011: A transitioning Arctic surface energy budget: The impacts of solar zenith angle, surface albedo and cloud radiative forcing. *Climate Dyn.*, **37**, 1643–1660, https://doi.org/10.1007/s00382-010-0937-5.

Serreze, M. C., and R. G. Barry, 2011: Processes and impacts of Arctic amplification: A research synthesis. *Global Planet. Change*, **77**, 85–96, https://doi.org/10.1016/j.gloplacha.2011.03.004.

——, A. Barrett, J. Stroeve, D. Kindig, and M. Holland, 2009: The emergence of surface-based Arctic amplification. *Cryosphere*, **3**, 11–19, https://doi.org/10.5194/tc-3-11-2009.

Shupe, M. D., and J. M. Intrieri, 2004: Cloud radiative forcing of the Arctic surface: The influence of cloud properties, surface albedo, and solar zenith angle. *J. Climate*, **17**, 616–628, https://doi.org/10.1175/1520-0442(2004)017<0616:CRFOTA>2.0.CO;2.

Sledd, A., and T. L'Ecuyer, 2019: How much do clouds mask the impacts of Arctic sea ice and snow cover variations? Different perspectives from observations and reanalyses. *Atmosphere*, **10**, 12, https://doi.org/10.3390/atmos10010012.

Soden, B. J., I. M. Held, R. Colman, K. M. Shell, J. T. Kiehl, and C. A. Shields, 2008: Quantifying climate feedbacks using radiative kernels. *J. Climate*, **21**, 3504–3520, https://doi.org/10.1175/2007JCLI2110.1.

Steele, M., W. Ermold, and J. Zhang, 2008: Arctic Ocean surface warming trends over the past 100 years. *Geophys. Res. Lett.*, **35**, L02614, https://doi.org/10.1029/2007GL031651.

Stephens, G. L., D. O'Brien, P. J. Webster, P. Pilewski, S. Kato, and J. Li, 2015: The albedo of Earth. *Rev. Geophys.*, **53**, 141–163, https://doi.org/10.1002/2014RG000449.

Stroeve, J. C., M. C. Serreze, M. M. Holland, J. E. Kay, J. Malanik, and A. P. Barrett, 2012: The Arctic's rapidly shrinking sea ice cover: A research synthesis. *Climatic Change*, **110**, 1005–1027, https://doi.org/10.1007/s10584-011-0101-1.

Tiao, G. C., and Coauthors, 1990: Effects of autocorrelation and temporal sampling schemes on estimates of trend and spatial correlation. *J. Geophys. Res.*, **95**, 20 507–20 517, https://doi.org/10.1029/JD095iD12p20507.

Tietsche, S., D. Notz, J. Jungclaus, and J. Marotzke, 2011: Recovery mechanisms of Arctic summer sea ice. *Geophys. Res. Lett.*, **38**, L02707, https://doi.org/10.1029/2010GL045698.

Vignesh, P. P., J. H. Jiang, P. Kishore, H. Su, T. Smay, N. Brighton, and I. Velicogna, 2020: Assessment of CMIP6 cloud fraction and comparison with satellite observations. *Earth Space Sci.*, **7**, e2019EA000975, https://doi.org/10.1029/2019EA000975.

Wang, X., J. Key, Y. Liu, C. Fowler, J. Maslanik, and M. Tschudi, 2012: Arctic climate variability and trends from satellite observations. *Adv. Meteor.*, **2012**, 505613, https://doi.org/10.1155/2012/505613.

Weatherhead, E. C., and Coauthors, 1998: Factors affecting the detection of trends: Statistical considerations and applications to environmental data. *J. Geophys. Res.*, **103**, 17 149–17 161, https://doi.org/10.1029/98JD00995.

Wielicki, B. A., and Coauthors, 2013: Achieving climate change absolute accuracy in orbit. *Bull. Amer. Meteor. Soc.*, **94**, 1519–1539, https://doi.org/10.1175/BAMS-D-12-00149.1.

Zelinka, M. D., T. A. Myers, D. T. McCoy, S. Po-Chedley, P. M. Caldwell, P. Ceppi, S. A. Klein, and K. E. Taylor, 2020: Causes of higher climate sensitivity in CMIP6 models. *Geophys. Res. Lett.*, **47**, e2019GL085782, https://doi.org/10.1029/2019GL085782.